



PAPER

Triboelectric effect based self-powered compact vibration sensor for predictive maintenance of industrial machineries

To cite this article: Hosangadi Prutvi Sagar *et al* 2021 *Meas. Sci. Technol.* **32** 095119

View the [article online](#) for updates and enhancements.

You may also like

- [Nanogenerator for scavenging low frequency vibrations](#)
Jae Yeong Park, Md Salauddin and M Salauddin Rasel
- [Self-powering vibration sensor based on a cantilever system with a single-electrode mode triboelectric nanogenerator](#)
Sagar Hosangadi Prutvi, Mallikarjuna Korrapati and Dipti Gupta
- [Progress of biomechanical energy harvesters for wearable electronic applications](#)
Hai-Tao Deng, Yi-Lin Wang, Dan-Liang Wen et al.

PRIME
PACIFIC RIM MEETING
ON ELECTROCHEMICAL
AND SOLID STATE SCIENCE

HONOLULU, HI
Oct 6–11, 2024

Abstract submission deadline:
April 12, 2024

Learn more and submit!

Joint Meeting of

The Electrochemical Society

•

The Electrochemical Society of Japan

•

Korea Electrochemical Society

A woman in a black jacket and yellow lanyard stands in front of a poster board at a conference booth. Another person is visible in the background looking at a poster.

Triboelectric effect based self-powered compact vibration sensor for predictive maintenance of industrial machineries

Hosangadi Prutvi Sagar¹, Sunil Meti², Udaya K Bhat²  and Dipti Gupta¹ 

¹ Metallurgical Engineering and Materials Science Department, Indian Institute of Technology Bombay, Mumbai 400076, India

² Metallurgical and Materials Engineering Department, National Institute of Technology Karnataka, Surathkal 575025, India

E-mail: diptig@iitb.ac.in

Received 12 December 2020, revised 7 February 2021

Accepted for publication 16 February 2021

Published 11 June 2021



Abstract

This article showcases a compact self-powered contact-mode triboelectric (TE) phenomenon-based vibration sensor for predictive maintenance of industrial machinery. The sensor has a suspended proof-mass that oscillates under external vibration and causes contact-separation between Teflon and zinc oxide (ZnO) films creating tribo signals, which are used for both sensing and powering mechanisms. For these sensors to be implemented in real-time applications, the sensor must be cost-effective, reliable, and repeatable. Hence, the active layer (ZnO film) is fabricated by an efficient process of microwave-assisted thermal decomposition followed by the established screen printing method. The sensor operates up to 400 Hz and is highly robust with no significant decay in signal strength even after 120 000 cycles tested at elevated stress values. The device produces a maximum voltage (V) of ± 30 V, short circuit current of $\pm 3 \mu A$, and can deliver a maximum power density of 0.5 W m^{-2} , at $8 \text{ M}\Omega$ load resistance. In the frequency domain, the device generates a maximum V at 55 Hz and can charge 1 μF capacitor to 3.5 V in 25 s. To demonstrate the functionality of the sensor in a real application, it is implemented on a lab-scale vacuum pump to capture the system faults by analyzing the harmonic signatures. Thus, in this article, we have showcased end-to-end development of the sensor from material synthesis to device testing along with its signal processing techniques and proved that the sensor can readily be implemented in industrial environments as is. This article thus emphasizes bridging the lab-to-market gap for TE devices as a self-powering sensor.

Supplementary material for this article is available [online](#)

Keywords: vibration sensor, condition monitoring, predictive maintenance, self-powering device, triboelectric effect

(Some figures may appear in colour only in the online journal)

List of abbreviations

TE:	Triboelectric	SP:	Screen-printing
PM:	Predictive maintenance	V:	Voltage
ZnO :	Zinc oxide	I_{sc} :	Short circuit current
NP:	Nanoparticle	CM:	Condition monitoring
μw :	Microwave	PTFE:	Teflon or poly(tetrafluoroethylene)
		KOH:	Potassium hydroxide
		DI:	De-ionized

PMMA:	Poly (methyl methacrylate) or acrylic
TENG:	Triboelectric nanogenerator
CAD:	Computer-aided design

1. Introduction

Predictive maintenance is becoming an important use-case for Industry 4.0 as it is enabling the manufacturers to reduce the unscheduled downtime by forecasting the failure of machine components and performing focused and timely maintenance. The tools/techniques for predictive maintenance are typically based on tool CM involving methods that are lately getting accompanied by machine learning (ML) and artificial intelligence (AI) methods [1]. Among several CM methods, such as vibration analysis, infrared (IR) imaging, oil analysis, physical observations, etc. Vibration analysis is a versatile technique that can be employed in almost all types of machines [2]. Here, the real-time periodic analysis of the harmonic response of the vibration signature of the machine helps in the evaluation and prediction of the machine's health.

The vibration sensors commonly used by industries are based on either battery-powered vibrating spring or piezoelectric material. Both of which are not suited for long term usage as the active material in both these sensors undergo continuous fatigue loading, causing performance degradation after prolonged usage [3, 4]. Incidentally, TE phenomenon-based devices can mitigate this problem as here the surface of two dissimilar materials come in contact which causes contact electrification and electrostatic induction in tandem [5, 6]. Since this phenomenon is proven to be dependent on the active surface area [7], the performance of the active film/membrane does not degrade despite the mechanical failures. TENG based vibration sensors thus have a strong potential to find usage in industries if they can be made lightweight, compact, and manufactured in a cost-effective and scalable way.

In this work, we have thus focused on fabricating a compact vibration sensor with a robust design, and works in a self-powered mode, while employing scalable fabrication technology such as SP and μ w decomposition technique. The vibration sensor works on the triboelectric phenomenon using Teflon and SP-ZnO as active layers. The Teflon (PTFE) is attached to the bottom surface of a seismic/proof mass (brass) which is suspended with an elastic band. When the entire structure is excited, the brass oscillates due to inertial effects that create contact and separation motion between the active layers producing the TE waveform. The sensor is thoroughly characterized first and then tested on an active lab scale vacuum pump to demonstrate its usability as a CM tool in real-time industrial scenarios.

Our vibration sensor is capable of measuring a wide range of mechanical vibrations without the need for any specialized mounting requirements [8, 9] such as magnetic mounting, precision alignments [10], and so on. This is an important parameter to consider to implement the sensor on conventional equipment that's already in use. Additionally, the reported vibration sensor is a passive device and does not affect the normal operations of the

machinery. The sensor is self-powering and does not require dedicated signal processing to integrate into the existing infrastructure.

2. Experiments

The vibration sensor has three major fabrication steps: (a) fabrication of tribo active layers (b) fabrication of housing and (c) fabrication of seismic mass. The complete step by step fabrication is shown in figure 1. Each of these fabrication procedures is further elaborated in detail below.

2.1. *ZnO synthesis*

0.5 M zinc nitrate hexahydrate ($Zn \cdot (NO_3)_2 \cdot 6(H_2O)$) is added to DI water and mechanically stirred for 30 min. 0.5 M KOH is gradually added to the above solution under continuous stirring. Finally, an ammonia solution (25%) is added dropwise under vigorous stirring for 30 min to maintain the pH between 10 and 11. The prepared solution is then poured into a beaker and kept in convection mode μ w-oven for 10 min at 700 W power. The solution is then cooled down to room temperature and washed with DI water and alcohol several times to remove the impurities. Finally, the solution is dried in a hot air oven at 60 °C for 24 h to obtain ZnO NPs.

2.2. *Paste preparation*

45 wt% (450 mg) of the obtained ZnO nano-powder is mixed with 5 wt% (50 mg) of ethylcellulose binder and 50 wt% (500 mg) of terpineol (solvent). This mixture is vigorously grounded in Mortar-pestle for 15 min, which results in a highly viscous agglomerate free ZnO paste for SP [11, 12]. A screen with #120 mesh is used to create the mask and used for SP. During the SP process, 5 to 10 mm of snap-off distance is used to ensure quick release of the screen without leaving any permanent texture on the wet film. Here, we used copper tape as an electrode, as the adhesive gum makes it easier for (flexible) assembling later on. The surface is solvent cleaned (i.e. cleaned with isopropyl alcohol, acetone, and DI water in exact order) and dried. It is then used as a substrate for SP. Further, the obtained film is dried under IR illumination for 2 h to completely evaporate the solvents. The obtained ZnO film has a 7 μ m thickness and roughness of 1 μ m as measured using the Dektak® profilometer.

2.3. *Device fabrication*

The vibration sensor assembly has two major parts. a rigid stationary part and an oscillating part. The rigid frame is fabricated using laser cut acrylic sheets (PMMA). Here, a 4 mm thick PMMA sheet is used for the bottom substrate, and an 8 mm thick sheet is used as structural support for the oscillating part. The SP-ZnO film adheres to the bottom acrylic substrate. This acts as a stationary tribo-positive layer. While for the counter tribo surface, the copper-cladded PTFE is pasted onto the machined brass block with PTFE

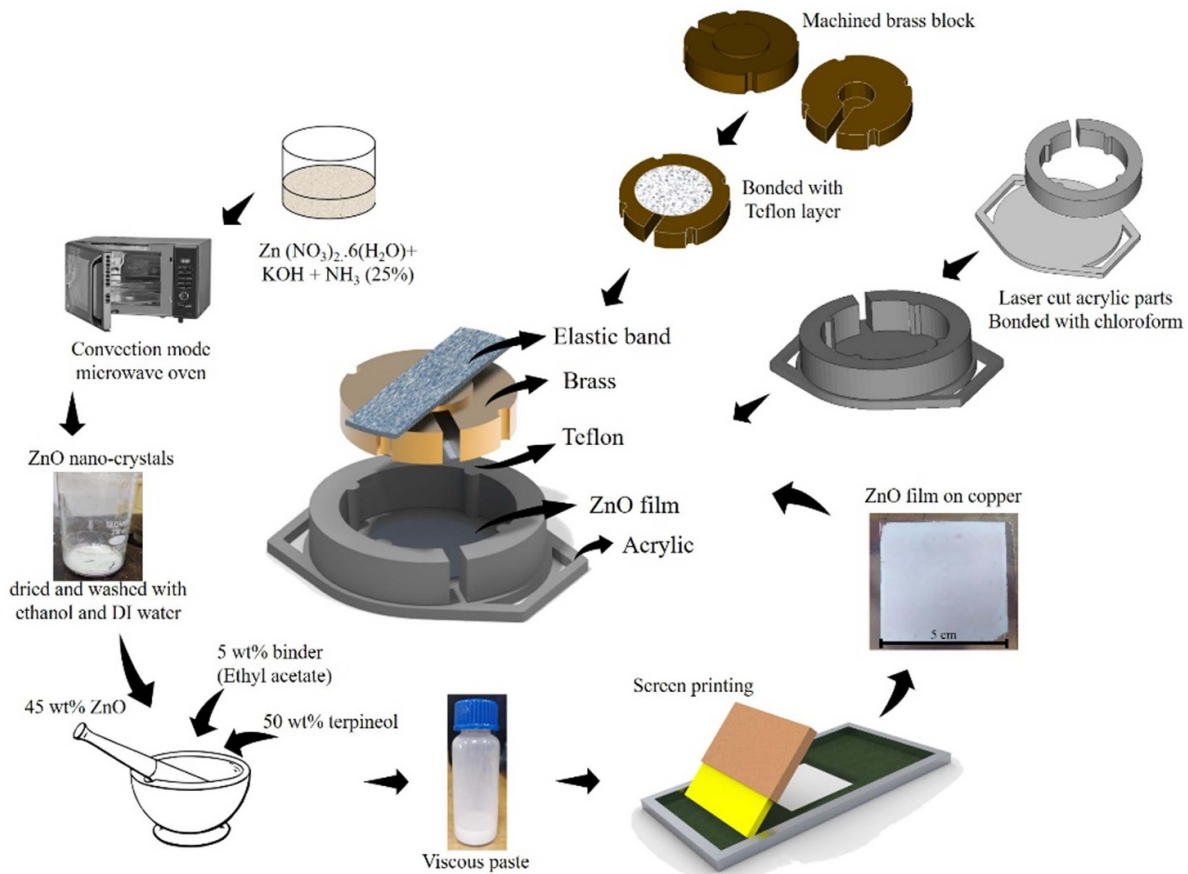


Figure 1. Pictogram showcasing the complete fabrication procedure of the vibration sensor.

exposed towards the ZnO film. The assembly is then suspended using a commercially available 180 gsm elastic band which is pre-stretched to $\approx 120\%$. Cyanoacrylate (Fevi kwik[®]) is used as a bonding agent between brass and elastic band, and the elastic band to the acrylic support member. Enough spacing is provided inside the brass block to compensate for the solder bumps so that the entire PTFE surface is smooth.

2.4. Characterization and testing

The x-ray diffraction is performed (XRD, Machine-Rigaku, Japan) with Cu-K α radiation ($\lambda = 1.5406 \text{ \AA}$) in the 2θ range from 5° to 80° . The scanning speed employed was 2° min^{-1} with a 0.02° step. Scanning electron microscopy (SEM) (carl-Zeiss Auriga compact) is used to examine the surface morphology of the ZnO NPs and ZnO film. The electrical performance (i.e. V and current output of the device) is tested using the Tektronix oscilloscope (DPO 2014B) and Keithley parameter analyzer (SCS 4200 A) respectively. The impedance of the oscilloscope for V measurements is $10 \text{ M}\Omega$. The elastic band is subjected to uniaxial tensile testing using Mark-10 universal tensile tester (model no. ESM 303). The oxide film's durability is tested on a motorized fixture built in-house (it is built using laser-cut PMMA sheets and 3D printed parts). Arduino platform is employed for data logging. The vibration

testing is performed on a vibration generator (Frederiksen 2185) along with a function generator (AFG 3022C). The experimental setup along with the schematic diagram is shown in figures 2(a) and (b) respectively. The audio waveforms of the device are captured using a commercial cell-phone placed approximately 5 cm away.

All the materials are used as procured and no additional surface modification techniques are implemented. The PTFE surface (exposed towards ZnO) is initially solvent cleaned using isopropyl alcohol (IPA), acetone, and DI water to preserve the integrity of the experiments. The screen-printed ZnO surface is used as prepared without any further treatment.

3. Results and discussions

The sensor has overall dimensions of $50 \times 42 \times 10 \text{ mm}$ with dry weight (i.e. without any additional mounting support) of 55 g. Figure 3(a) shows the vibration sensor held in the palm, showing its compact structure. Figure 3(b) shows its CAD model along with its constituent components. Here, Teflon is chosen as the dielectric surface in tandem with SP-ZnO film [11]. These tribo-active layers, i.e. Teflon and SP-ZnO are 0.1 mm and $1 \mu\text{m}$ in thickness, respectively. The sensor has a 23 mm diameter overlap area between the active layers. The sensor has a precision-machined brass mass (weights 30 g) suspended by a commercial elastic band (180 gsm) which

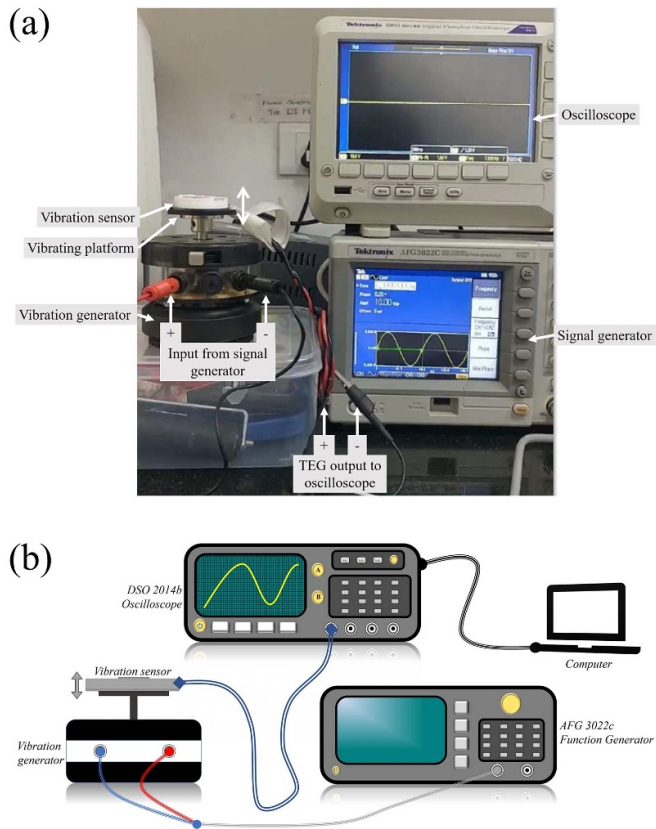


Figure 2. (a) Experimental setup of the vibration test setup.
(b) Schematic diagram of the vibration test setup.

oscillates when the base is excited by any external forces due to its inertia. The brass is allowed to oscillate freely in only the ‘out-of-plane’ direction (i.e. perpendicular to the base). Other degrees of freedom (i.e. pitching, rolling, and yawning) are constrained by the cylindrical guideways machined. These details are highlighted in figure 3(b). When the sensor’s base is excited by an external vibration source, because of the device’s architecture, the brass oscillates and starts hitting the ZnO surface. Thus, causing the continuous contact separation action at the PTFE-SP-ZnO heterojunction creating tribo-signals, making it a contact mode triboelectric device. The detailed signal generation process is explained in the next section.

Figures 3(c) and (d) are the micrograph of the as-synthesized ZnO NPs and SP-ZnO film respectively. From these images, it is observed that the obtained NPs are uniform and are evenly sized. The SP-ZnO film is devoid of any pin-holes and is uniform over a large area. The micrograph shows that the SP-ZnO film has inherent micro texturing (grass-like texture), produced without any secondary surface treatments. Since the triboelectric phenomenon is surface area dependant, using a single-step approach to produce large-area surface texturing is beneficial for the device’s performance. The material characterization (XRD) of the film and NPs is reported in SI, which proves that the obtained NPs and screen-printed ZnO film does not have any other phases or impurities and are

contaminant free. The characteristic diffraction peaks of ZnO [13–16] are well-differentiated in both NPs and film’s spectrum. We also perform the Rietveld refinement analysis to find out the lattice parameters of the ZnO and the obtained values are in good agreement with the theoretical values (S1).

3.1. Structural analysis of the vibration sensor

Since the brass is continuously oscillating, the elastic band is always subjected to fully reversed cyclic loads. To visualize these stresses and to obtain the mechanical response of the device, the sensor is simulated in the finite element environment using LS-DYNA, and ANSA software. Here, the materials used are linear elastic materials except for the elastic band. The elastic band is a hyper-elastic material and employed in its pre-stretched state (i.e. $\approx 120\%$ pre-stretched). Hence, the Mooney-Rivlin 9 parameter material model [17, 18] is implemented to define its mechanical properties. The elastic band of 40 mm (L) \times 10 mm (W) \times 1 mm (T) is subjected to a uniaxial tension test and the obtained stress-strain plot is shown in figure S2 (available online at stacks.iop.org/MST/32/095119/mmedia). The fitted Mooney Rivlin parameters (using Ansys[®]) are tabulated in table S2. The mechanical properties of brass and PMMA used for the simulations are listed in table S3. The boundary conditions employed are shown in figure S4.

3.1.1. Static and dynamic analysis (simulations). We used LS-DYNA to analyze impact conditions, since it is a suitable environment to test the impact forces without getting into any of the simulation complications such as convergence errors, mesh deformations, etc. We imposed 30 Hz sinusoidal vibration with 1 mm amplitude on the sensor’s baseplate which creates an oscillation motion in the brass. The stresses developed in the elastic band is shown in figure 4(a). The maximum stress developed in the elastic band is found to be 46 kPa, which is well within its elastic limits [19]. The displacement of the brass block in the y-direction and the interface forces generated between SP-ZnO and PTFE is shown in figure 4(b). this interface force reaches a peak load of 16 gf when the brass block strikes the acrylic base.

These simulations indicate that the stresses developed on the ZnO surface appear to be randomly distributed but localized in nature (as shown in figure 4(c)). A similar erosion pattern is observed after the film is physically tested (as shown in figure 4(d)). This stress concentration is due to the flexible nature of the Teflon film coming in contact with the ZnO film when the brass hits. Since the central portion of the brass has a hollow cut-out to enable the wires to come out, the stresses are low at the center. This causes the Teflon to relax locally upon impact and causes the stress concentration regions to be distributed on the interface area.

3.1.2. Durability tests for the TENG active layers. Since the TENG heterojunction is subjected to constant impulse loads, the film reliability is of paramount importance for long shelf life. Hence, it is tested for durability using an in-house built

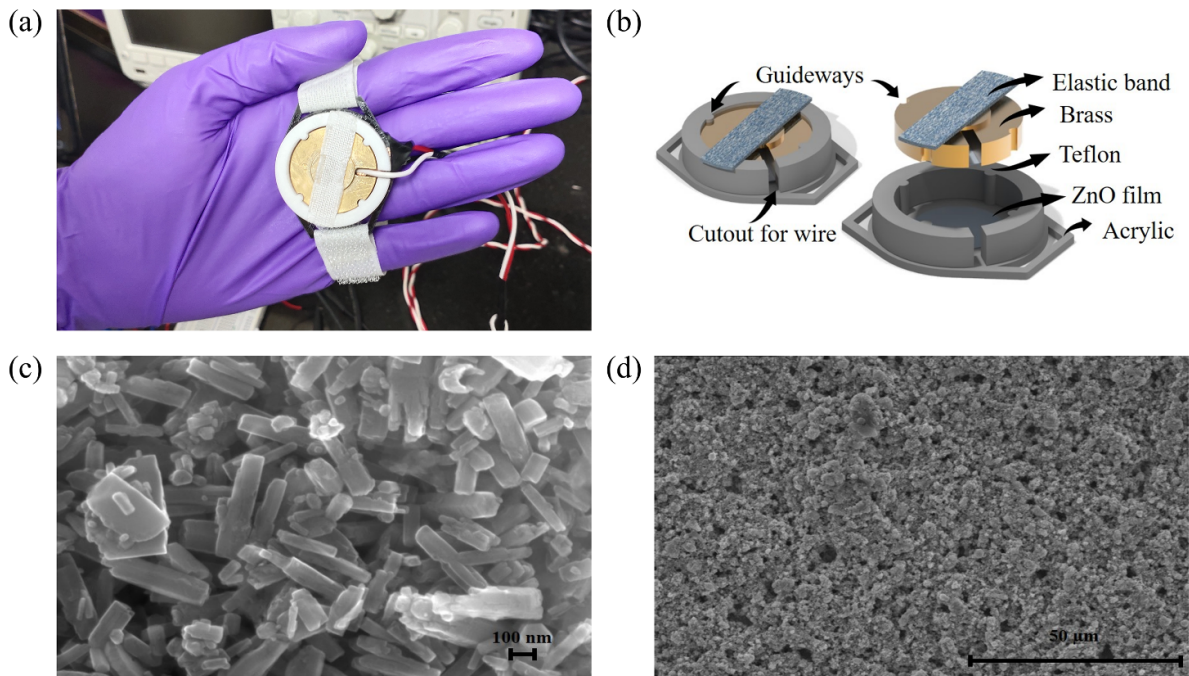


Figure 3. (a) Vibration sensor held in the palm, showing its compact structure, (b) CAD model of the vibration sensor along with its exploded view showing the constituent components, (c) and (d) SEM micrograph of the as-synthesized ZnO nanoparticles and SP-ZnO film respectively.

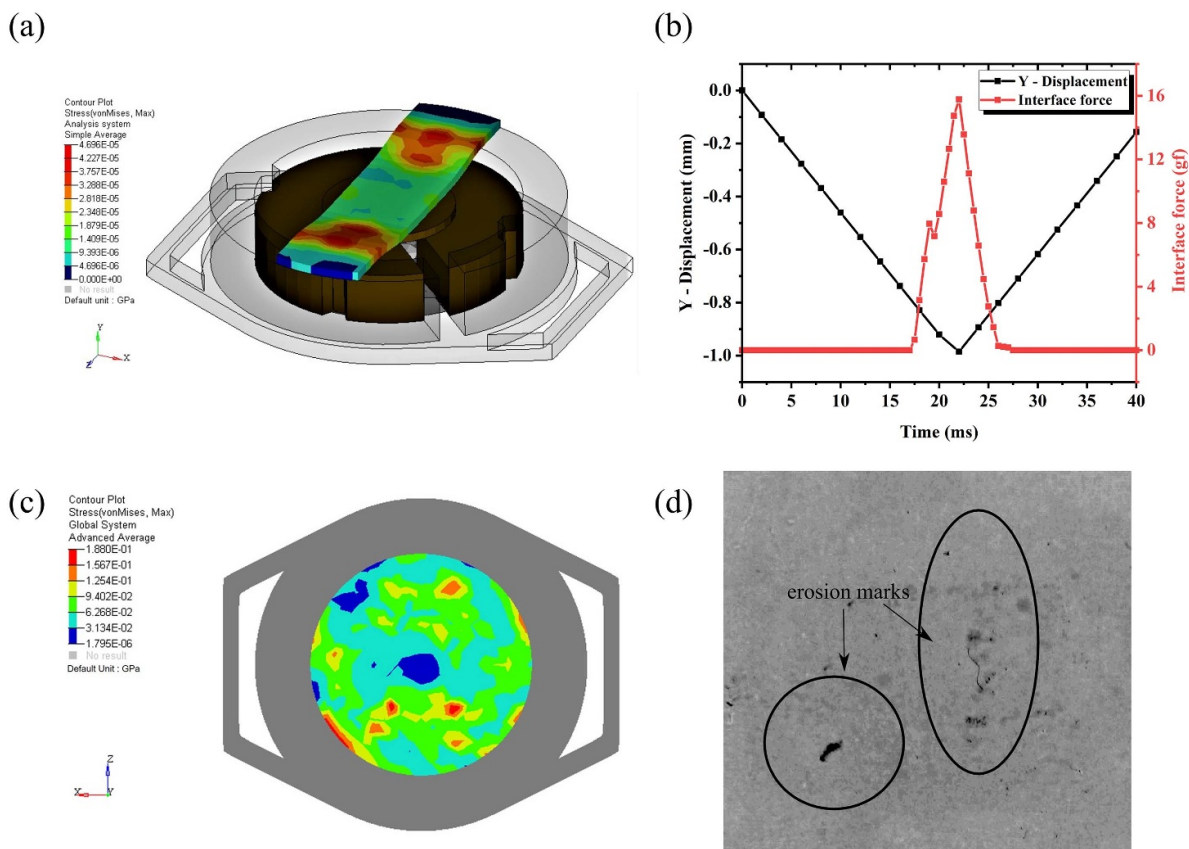


Figure 4. Structural analysis of the vibration sensor. (a) Stress developed in the elastic band when brass travels the entire gap (1 mm displacement), (b) y-axis displacement of the brass, and the interface forces generated when brass/Teflon hits the SP-ZnO surface, (c) stress pattern developed on SP-ZnO surface after impact loading and (d) image showing the ZnO surface eroded after being continuously used for >100 000 pulses.

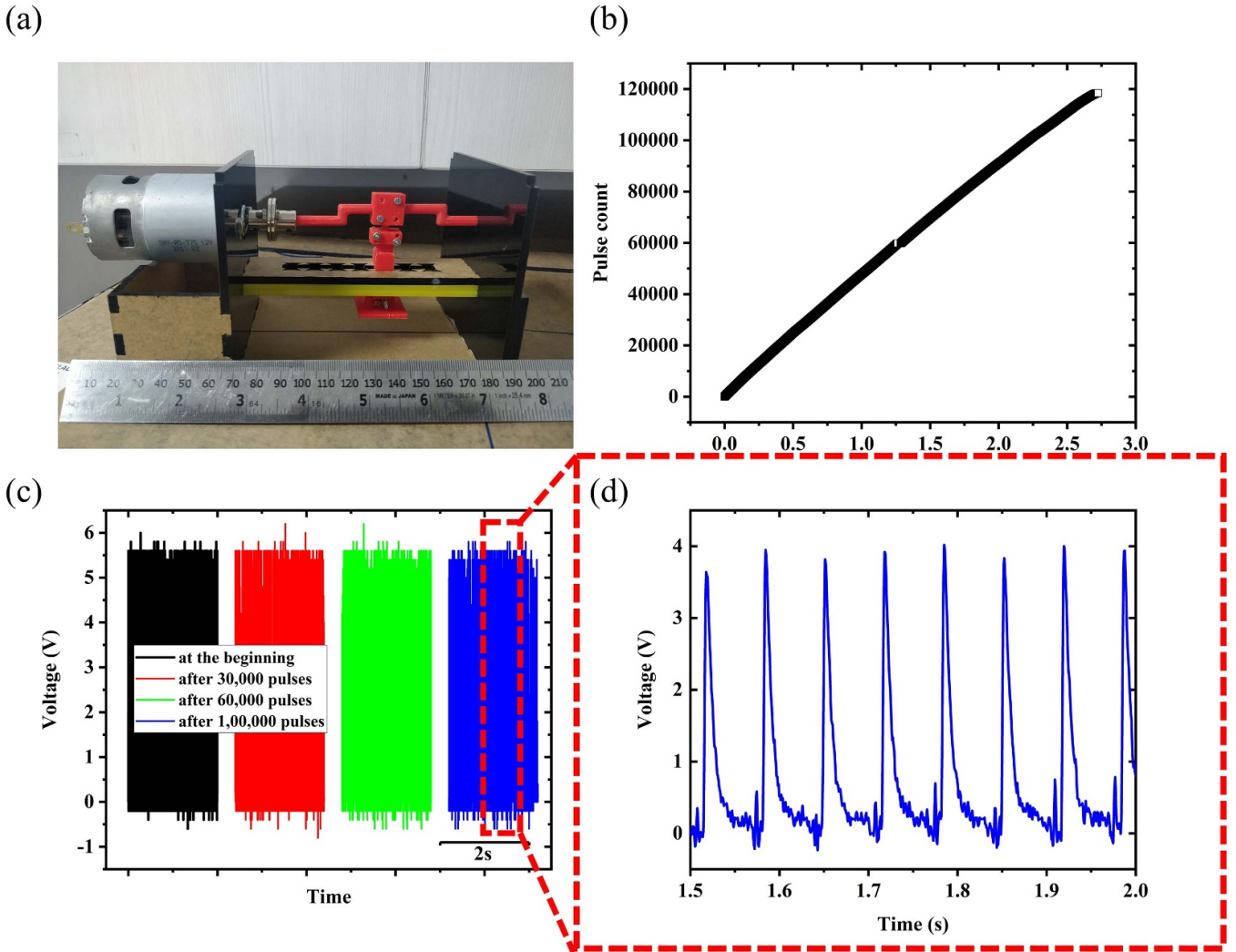


Figure 5. Durability tests for the TENG active layers (a) motorized fixture for testing the durability, (b) triboelectric pulse count which demonstrates the durability of the oxide film, (c) voltage waveform at the beginning, after 30 000 pulses, after 60 000 pulses, and after 100 000 pulses and (d) detailed voltage waveform which showcases well-resolved peaks.

motorized fixture as shown in figure 5(a). The testing fixture is made of laser-cut rigid acrylic sheets for outer structural parts and polylactic acid (PLA)-based 3D-printed parts to convert the rotary motion from DC motor to reciprocating motion. This setup generates a maximum displacement of ~ 10 mm. The PTFE is attached to the motor fixture, while the SP-ZnO is held stationary. The testing is performed in ambient conditions (i.e. temperature and relative humidity at the time of testing was 32 °C and 56% RH resp.) without any specialized environmental regulations. The fixture applies a normal load of 300 gf (measured using a porous sponge of known stiffness) at 15 Hz at the heterojunction. This testing load is $18.75 \times$ the interface forces generated during the actual sensor operation ($300 \text{ gf}/16 \text{ gf} = 18.75$). It is found that while testing at higher loads, the ZnO film is fully functional even after 120 000 cycles of operations with negligible decay in the device performance (as shown in figures 5(b) and (c)). Neither ZnO nor PTFE showed any considerable physical damages other than regular erosion marks (as shown in figure 4(d)). Figure 5(b) highlights that the testing is performed continuously for 2.5 h,

(albeit a 5 min gap was provided during testing after 1.5 h for the PLA parts to cool down, which tend to soften under frictional heat generated while operating). Figure 5(c) showcases that the V amplitude is consistent throughout. Snippets of the V waveform are captured at various intervals of the operation i.e. measured at the beginning of the experiment, after 30 000 pulses, after 60 000 pulses, and after 100 000 pulses, respectively. Figure 5(d) shows the zoomed-in image of the V waveform depicting its near-constant amplitude even after 120 000 cycles of operations. Since the durability testing is performed at higher loads than the actual loads generated while normal operation, it ensures that the film is reliable enough to be used in real-time industrial applications. Here, the data logging is performed by using Arduino (the detailed circuitry is explained in section 3.2).

3.2. Triboelectric performance evaluation

The working principle of contact mode TENG devices is well explained in the earlier reports [20–22] and also depicted

in figure 6(a). As the two active surfaces come in contact and separate, the surface charges (i.e. electrons) gets pulled from material with less electron affinity to the material with higher electron affinity [23–25]. This causes electric charges to get decorated on the interface surfaces [26]. Since the tribo active materials are insulators in nature, the charges become immobilized and are denoted as static charges [27–29]. These static charges create an electric field around it which induces mirror charges on their respective backing electrode. This phenomenon creates a potential difference between the two electrodes in the external circuit and causes a burst of electrons to flow from one electrode to another. When these mating surfaces come back in contact, the established electric field collapses, and the potential difference between the electrodes collapse. Hence there will be a reverse flow of charges to bring equilibrium between them. Thus, a single contact separation causes electrons to flow in the external circuit. This cyclic process is clearly explained in figure 6 (a(i)–(iv)). Thus, it is defined as a self-powered device. The generated V waveform is as shown in figure 6(b).

The vibration sensor produces a maximum V of 68 V (peak to peak) [30–32], I_{sc} (peak to peak) of 8.88 μ A, and maximum transfer charge of 25 nC (as shown in figures 6(c)–(e)) respectively. The device yields a maximum power of 0.225 mW at load resistance of 8 M Ω (figure 6(f)). Corresponding power density is calculated to be 0.5 W m⁻². The power density is calculated by normalizing the maximum power obtained with the overlap area. This obtained power density is comparable to similar reported results [33]. We charged 1 μ F and 10 μ F capacitor using the circuit shown in figure 6(g) to 3.5 V in under 25 s and 200 s, respectively (shown in figure 6(h)).

Since the output of the TENG device is an alternating pulsed waveform, the signal is first rectified using a commercial full-wave rectifier DB107 before charging the capacitors. The output after rectification is then fed to the capacitor. The RC filter has $R = 10$ M Ω and $C = 1$ μ F and 10 μ F respectively. These values are chosen to match the output impedance of the TENG device to the electrical circuit connected (load matching). Arduino is utilized for pulse counting during the durability testing of the active layers. Here to avoid Arduino board failures from large Vs surges from the TENG device, the output of the device is first reduced to <5 V (figure 5(d)) using the same circuit figure 6(g) and then fed to Arduino analog pins. Here we employed AEC104 ceramic capacitors instead of large capacitors as they could reach 3.5–4 V instantaneously without any time delays.

3.3. Vibration testing

To measure the harmonic response of the sensor, it is tested on a vibration generator and excited using sine waves. The detailed experimental setup is discussed in the experimental section. The TENG device is tested up to 800 Hz and its

peak-to-peak V output is shown in figure 7(a). Up to 60 Hz, the peak-to-peak V is prominent and beyond 60 Hz the amplitude reduces drastically. This is attributed to the mode change from contact mode to non-contact mode, at 60 Hz. The mode change is proven by measuring the audio signal strength as shown in figure 7(b). In contact mode of operation (i.e. up to 60 Hz), the peak-to-peak V varies continuously and is maximum when the device resonates. Hence the sharp peaks are observed at 30 Hz and 55 Hz. In the non-contact mode of operation (i.e. beyond 60 Hz), as the frequency is increased the V output drops continuously since the displacement of the brass is also reduced. In contact mode (the sample audio is captured at 42 Hz), the audio recording shows a characteristic tapping sound. While in non-contact mode (the sample audio is captured at 70 Hz), the sensor produces high pitched sound without any tapping sound. These audio files can be found in the supporting information (files names ESM_1_60 Hz and ESM_2_72 Hz).

The percentage error is shown in figure 7(c) gives the linear operating bandwidth of the sensor. It is calculated as per equation (1). The output frequency is obtained by subjecting the raw time-domain V waveform to Fourier transformation. From the list of obtained frequencies, the frequency value closest to the input frequency is selected and used as the output frequency. From this percentage error plot figure 7(d), it is clear that the sensor can be used as a good vibration sensor from 0 to 400 Hz wherein there is a negligible error (<0.2%) and the input frequency is reproduced accurately. Since most of the industrial instruments operate below 400 Hz, the sensor can be employed in all conventional types of machinery effectively. Beyond 400 Hz, it is observed that the peak-to-peak V becomes negligible and the errors become larger:

$$\% \text{Error} = \frac{\text{Input freq} - \text{prominent freq}}{\text{Input freq}} \times 100. \quad (1)$$

Now, to measure the sensitivity of the vibration sensor, it is mounted on the vibration generator along with a standard accelerometer. The peak-to-peak V of the vibration sensor is normalized with the accelerometer ‘g’ readings and the obtained sensitivity is as shown in figure 7(e). The results show that the sensor is highly sensitive as compared to other commercially available vibration sensors on the market depicted in table 1. The sensitivity profile of our sensor follows the same contour as that of the peak to peak V response. This is attributed to large V values produced by the TENG mechanism. The vibration sensor is found to be highly sensitive at 55 Hz with a sensitivity of 46.9 V g⁻¹.

3.4. Health monitoring of a pump

To prove the usability and showcase the system readiness level, as a proof of concept the sensor is tested on a lab-scale 1/8 hp vacuum pump (GAST, model number: DOA-P725-BN)

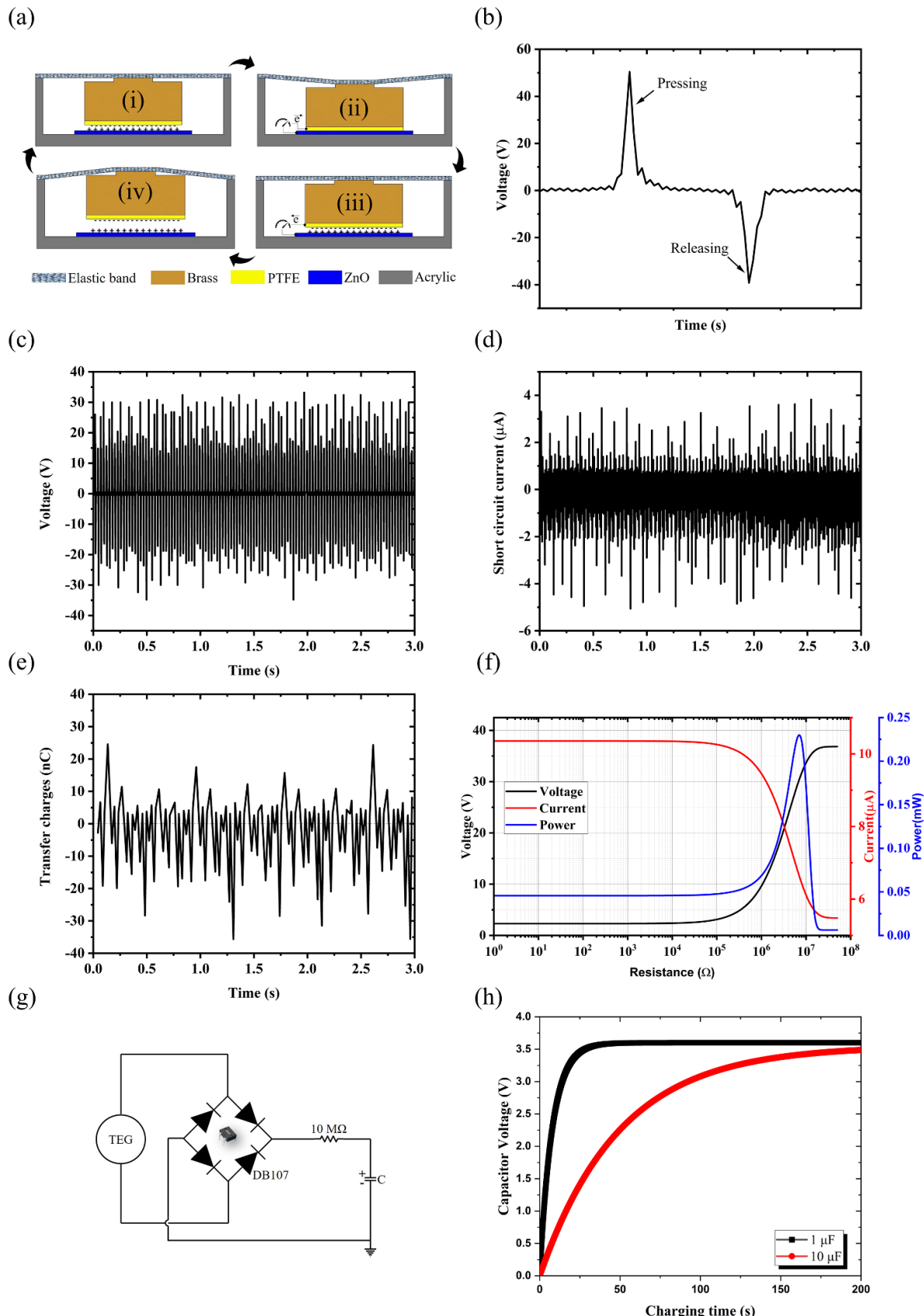


Figure 6. (a) Working principle of contact-separation mode triboelectric device. (b) The typical voltage waveform of the contact mode triboelectric device. (c) Voltage, (d) short circuit current, (e) transferred charge, (f) maximum power by load matching, (g) TENG interface circuit using DB107 full-wave rectifier and RC filter, and (h) capacitor charging using TENG device operated at 55 Hz.

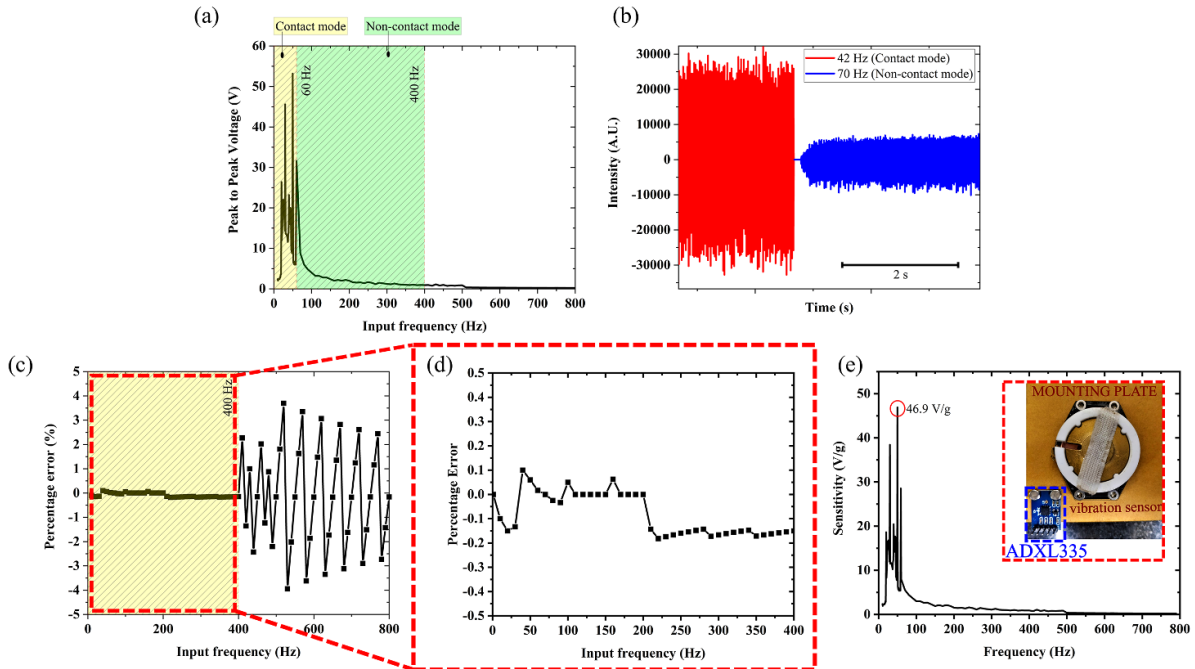


Figure 7. Vibration response of the TENG device under sine wave excitation for up-to 800 Hz (a) frequency domain peak to peak open-circuit voltage identifying contact and non-contact mode operations. In the contact mode regime, 30 Hz and 55 Hz peaks are visible (b) audio signal strength of the vibration sensor subjected to 42 Hz (contact mode) and 70 Hz (non-contact mode) input excitation and (c) error plot showcasing the operating regime of the vibration sensor. (d) Highlighted linear operating regime of the sensor showing <0.2% error variations. (e) The sensitivity of the vibration sensor was obtained by correlating the peak to peak voltage with ADXL335 accelerometer readings. The inset image shows the accelerometer mounted along with the vibration sensor.

Table 1. Comparison of our sensor with commercial piezoelectric based vibration sensors [34, 35].

Features	Our sensor	Commercial vibration sensor
Mounting	Easy to install	Requires magnetic mounting
Power supply	Self-powering	18–30 VDC
Sensitivity	46.9 V g ⁻¹	10 mV g ⁻¹
Frequency range	0–400 Hz	3.3–3000 Hz
Connector	Generic wires	Requires triaxial cables
Working principle	Triboelectric effect	Piezoelectric effect
Sensing element actuation	Contact separation	Shearing
Housing	Acrylic	Titanium
Directionality	Unidirectional	3 axis

as shown in figure 8(a). The sensor is mounted using regular double-sided self-adhesive tape on a clean surface without any specialized mounting features or preparations. When the pump is turned on, the motor rotation causes the entire body of the pump to vibrate, which activates the sensor mounted on the surface. This vibration creates an oscillation in the brass block and generates a triboelectric signal. The generated V waveform is shown in figure 8(b). This unprocessed raw signal when subjected to Fourier transformation analysis

yields, its constituent wavelets (as shown in figure 8(c) (stable mounting)). From this frequency spectrum peaks, we can see that the vibration sensor has captured the operating speeds of the pump (at 24 Hz) accurately. The frequency peaks captured at 48 Hz, 72 Hz, and 96 Hz are the 2nd, 3rd, and 4th multipliers (modes) of the rated speed (the demonstration video can be found in SI with file name ESM_3_pump mounting).

To showcase that the sensor can detect the system abnormalities, we induced an artificial fault in the motor (an unbalanced foundation). We placed standard 8 mm acrylic spacers under one of the legs. This causes the leg to be elevated (w.r.t. other legs) and induces an imbalance in the system, creating air gap eccentricity in the shaft and bearing link. This imbalance is mainly attributed to the shift in the center of gravity of the pump. As this imbalance is increased further, the eccentricity continues to grow [36], which is visible in the cascade spectra figure 8(c). Here, we can see that the amplitude of the peaks corresponding to the motor running speed is increasing with the increase in spacer height. The maximum change (of +22 dB) is observed for a peak at 24 Hz. It is calculated using equation 2:

$$Db = 20 \times \log_{10} \left(\frac{N_1}{N_2} \right) \quad (2)$$

where N_2 is the reference vibration magnitude and N_1 is the final vibration magnitude.

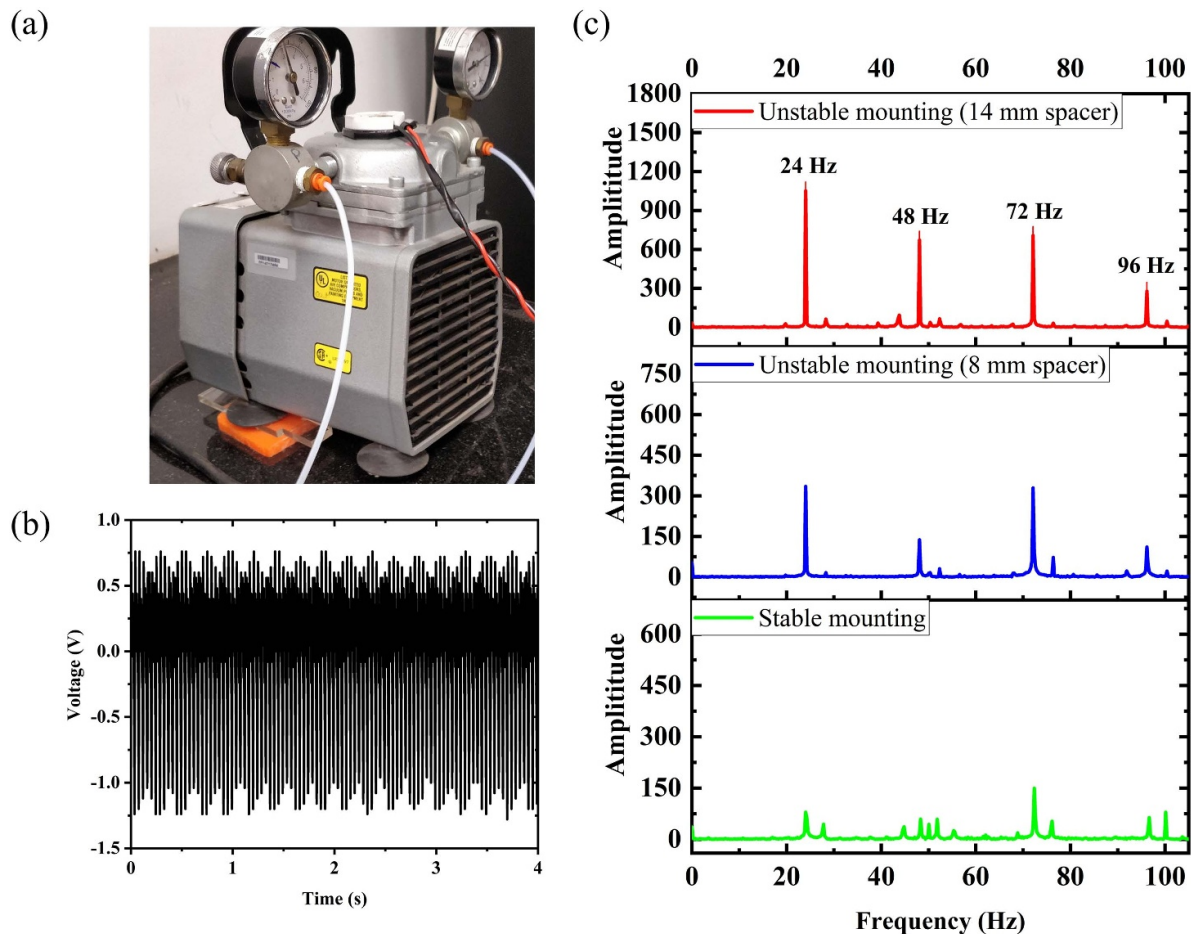


Figure 8. Vibration sensor mounted on the vacuum pump (GAST, DOA-P725-BN, 1/8 hp) with unstable foundation, (b) harmonic signature of the vacuum pump captured by the sensor and (c) FFT of the captured harmonic signature captured with stable both stable and unstable foundation (8 mm and 14 mm respectively).

4. Conclusion

In this article, a compact self-powering vibration sensor is successfully designed and implemented by using contact mode triboelectric effect. This sensor can passively capture the harmonics developed in the machinery, which can be post-processed for extracting useful information such as operation speeds. It is designed to keep cost-effectiveness and large-scale production as the design backbone to smoothen the large-scale implementation. This sensor can strongly assist in predictive maintenance techniques in any industrial environment owing to its robust design, simpler operations, and wide operating bandwidth (of up to 400 Hz) which covers most devices. Since this device could charge a capacitor easily (1 μ F capacitor to 3.5 V in 25 s) it shows the potential to be used as a continuous power source for the electronics, essentially making it a self-powering sensor. As the sensor shows the constant output for >120 000 cycles even at higher stress values, the sensor is highly robust and reliable. Since the sensor captured the pump operations accurately. It indicates that the sensor is ready to be employed in

real-life applications as-is. The generated harmonics are rich in information (such as operating speed, natural frequency, and so on) by amalgamating this with the advanced AI and ML concepts, this sensor can be converted into a powerful node in the vast internet of things network of an industrial environment to draw independent signals and could prove useful in the long run.

In our article, as a case study, we have detected faulty foundation, by observing the changes in peak amplitude, corresponding to the rated operating speeds in the FFT spectrum. Other faults such as faulty bearings, gear misalignment, oil depletion, and so on do not allow the machinery to run smoothly and changes the operating speeds considerably. This could easily be detected as peak shifts in the FFT spectrum or these faults could even develop newer peaks. A set of standard protocols can be developed and the resulting changes in the FFT peaks can be correlated to known faults. By training AI and ML algorithms to detect these subtle changes in real-time, continuous monitoring could be automated, leading to early detection of the probable defects in the system and avoiding unplanned shutdowns.

Acknowledgments

The authors would like to acknowledge the TCTD lab and Tinkerers' lab at IITB for their support towards prototyping. The authors would also like to appreciate the technical guidance provided by Professor Siddhartha Thallur.

Funding

This work is partially supported by the Department of Science and Technology, Government of India (RD/0119-DSTIM00-007) and Indian Space Research Organization (ISRO) (RD/0119-ISROC00-018).

Conflict of interest

The authors declare that they have no competing interests (financial or otherwise).

ORCID iDs

Udaya K Bhat  <https://orcid.org/0000-0002-0752-3600>
Dipti Gupta  <https://orcid.org/0000-0003-3252-3407>

References

- [1] Chuprina R 2020 The complete guide to predictive maintenance with machine learning (SPD Gr)
- [2] Kirankumar M V, Lokesha M, Kumar S and Kumar A 2018 Review on condition monitoring of bearings using vibration analysis techniques *IOP Conf. Ser.: Mater. Sci. Eng.* **376** 012110
- [3] Chen X, Luo L, Zeng Z, Jiao J, Shehzad M, Yuan G, Luo H and Wang Y 2020 Bio-inspired flexible vibration visualization sensor based on piezo-electrochromic effect *J. Mater.* **6** 643–50
- [4] Kobayashi T, Okada H, Masuda T, Maeda R and Itoh T 2011 A digital output accelerometer using MEMS-based piezoelectric accelerometers and arrayed CMOS inverters with satellite capacitors *Smart Mater. Struct.* **20** 065017
- [5] Seol M L, Lee S H, Han J W, Kim D, Cho G H and Choi Y K 2015 Impact of contact pressure on output voltage of triboelectric nanogenerator based on deformation of interfacial structures *Nano Energy* **17** 63–71
- [6] Lowell J and Rose-Innes A C 1980 Contact electrification *Adv. Phys.* **29** 947–1023
- [7] Niu S, Wang S, Lin L, Liu Y, Zhou Y S, Hu Y and Wang Z L 2013 Theoretical study of contact-mode triboelectric nanogenerators as an effective power source *Energy Environ. Sci.* **6** 3576
- [8] Jiang Q and Yang M 2013 Simulation and experimental study of a three-axis fiber Bragg grating accelerometer based on the pull-push mechanism *Meas. Sci. Technol.* **24** 115105
- [9] Lee Y G, Kim D H and Kim C G 2012 Performance of a single reflective grating-based fiber optic accelerometer *Meas. Sci. Technol.* **23** 045101
- [10] De Freitas J M, Wooler J P F and Nash P J 2006 Measurement of sensor axis misalignment in fibre-optic accelerometers *Meas. Sci. Technol.* **17** 1819–25
- [11] Kartikay P, Yella A and Mallik S 2020 Binder-solvent effects on low temperature-processed carbon-based, hole-transport layer free perovskite solar cells *Mater. Chem. Phys.* **256** 123594
- [12] Dubourg G and Radović M 2019 Multifunctional screen-printed TiO₂ nanoparticles tuned by laser irradiation for a flexible and scalable UV detector and room-temperature ethanol sensor *ACS Appl. Mater. Interfaces* **11** 6257–66
- [13] Wang J, Wang Z, Huang B, Ma Y, Liu Y, Qin X, Zhang X and Dai Y 2012 Oxygen vacancy induced band-gap narrowing and enhanced visible light photocatalytic activity of ZnO *ACS Appl. Mater. Interfaces* **4** 4024–30
- [14] Meti S, Rahman M R, Ahmad M I and Bhat K U 2018 Chemical free synthesis of graphene oxide in the preparation of reduced graphene oxide-zinc oxide nanocomposite with improved photocatalytic properties *Appl. Surf. Sci.* **451** 67–75
- [15] Nipane S V, Korake P V and Gokavi G S 2015 Graphene-zinc oxide nanorod nanocomposite as photocatalyst for enhanced degradation of dyes under UV light irradiation *Ceram. Int.* **41** 4549–57
- [16] Qurashi A, Tabet N, Faiz M and Yamzaki T 2009 Ultra-fast microwave synthesis of ZnO nanowires and their dynamic response toward hydrogen gas *Nanoscale Res. Lett.* **4** 948–54
- [17] Mooney M 1940 A theory of large elastic deformation *J. Appl. Phys.* **11** 582–92
- [18] Model C, Model H, Model M, Model M, Parameter M, Stretch P and Energy S 2015 *Mooney-Rivlin Model*
- [19] Byun J H and Chou T-W 2000 Mechanics of textile composites *Compr. Compos. Mater.* **1** 719–61
- [20] Niu S, Liu Y, Wang S, Lin L, Zhou Y S, Hu Y and Wang Z L 2013 Theory of sliding-mode triboelectric nanogenerators *Adv. Mater.* **25** 6184–93
- [21] Jiang T, Chen X, Yang K, Han C, Tang W and Wang Z L 2016 Theoretical study on rotary-sliding disk triboelectric nanogenerators in contact and non-contact modes *Nano Res.* **9** 1057–70
- [22] Niu S, Wang S, Liu Y, Zhou Y S, Lin L, Hu Y, Pradel K C and Wang Z L 2014 A theoretical study of grating structured triboelectric nanogenerators *Energy Environ. Sci.* **7** 2339–49
- [23] Meunier M and Quirke N 2000 Molecular modeling of electron trapping in polymer insulators *J. Chem. Phys.* **113** 369–76
- [24] Davies D K 1969 Charge generation on dielectric surfaces *J. Phys. D: Appl. Phys.* **2** 1533
- [25] Wang Z L 2017 On Maxwell's displacement current for energy and sensors: the origin of nanogenerators *Mater. Today* **20** 74–82
- [26] Kim D, Tcho I-W, Jin I K, Park S J, Jeon S B, Kim W G, Cho H-S, Lee H S, Jeoung S C and Choi Y K 2017 Direct-laser-patterned friction layer for the output enhancement of a triboelectric nanogenerator *Nano Energy* **35** 379–86
- [27] McCarty L S and Whitesides G M 2008 Electrostatic charging due to separation of ions at interfaces: contact electrification of ionic electrets *Angew. Chem. Int. Ed.* **47** 2188–207
- [28] Lin L, Xie Y, Niu S, Wang S, Yang P K and Wang Z L 2015 Robust triboelectric nanogenerator based on rolling electrification and electrostatic induction at an instantaneous energy conversion efficiency of ~55% *ACS Nano* **9** 922–30
- [29] Bao Han C, Du W, Zhang C, Tang W, Zhang L and Lin Wang Z 2014 Harvesting energy from automobile brake in contact and non-contact mode by conjunction of triboelectrification and electrostatic-induction processes *Nano Energy* **6** 59–65
- [30] Salauddin M, Rana S M S, Sharifuzzaman M, Rahman M T, Park C, Cho H, Maharjan P, Bhatta T and Park J Y 2020 A

- novel MXene/Ecoflex nanocomposite-coated fabric as a highly negative and stable friction layer for high-output triboelectric nanogenerators *Adv. Energy Mater.* **11** 2002832
- [31] Shi Q and Lee C 2019 Self-powered bio-inspired spider-net-coding interface using single-electrode triboelectric nanogenerator *Adv. Sci.* **6** 1900617
- [32] Shi Q, Wu H, Wang H, Wu H and Lee C 2017 Self-powered gyroscope ball using a triboelectric mechanism *Adv. Energy Mater.* **7** 1701300
- [33] Narasimulu A A *et al* 2017 Significant triboelectric enhancement using interfacial piezoelectric ZnO nanosheet layer *Nano Energy* **40** 471–80
- [34] Dollenmeier GMBH 2021 *Vibration meters*
- [35] Dytran Instruments I 2021 *Noise, Vibration and Harshness (NVH)*
- [36] Correa J C A J and Guzman A A L 2020 *Mechanical Vibrations and Conditional Monitoring* vol 7 (Amsterdam: Elsevier)